ES Materials and Manufacturing
DOI: https://dx.doi.org/10.30919/mm1777

From Gold Mining Waste to Functional Sorbents: Structural and Compositional Insights into Copper Adsorption Efficiency

Arailym Kalymbet,[1,*] Sholpan Kubekova,[1,*] Victoria Kapralova[1] and Silviya Lavrova[2]

Abstract

This study explores the transformation of Akbakay gold ore waste into effective sorbents for heavy metal removal through phosphoric acid modification (20–35 wt.%) and thermal treatment at temperatures ranging from 400 to 800 °C. A range of characterization techniques—including XRD, EPMA, FTIR, SEM, BET surface area analysis, and zeta potential measurements—revealed notable structural changes. These included the formation of phosphate phases (such as lipscombite), increased porosity, surface fragmentation, and a more negative surface charge (up to −20.1 mV). Among the samples, the one treated at 600 °C with 20 wt.% acid (Sample 3) demonstrated outstanding Cu^{2+} removal efficiency (>97 %) across initial concentrations of 1–40 mg/L, achieving a maximum adsorption capacity of 1.33 mg/g. The adsorption behavior followed the Langmuir isotherm model, indicating monolayer adsorption on a uniform surface. Kinetic analysis showed rapid metal uptake, with over 99 % removal within 120 minutes, best described by a mixed-order model that reflects both physical and chemical adsorption mechanisms. Fixed-bed column experiments further confirmed the material's performance, achieving a dynamic capacity of 0.847 mg/g and over 83 % Cu^{2+} removal. Breakthrough occurred at approximately 25 mL, with no 95 % breakthrough observed even at 300 mL. Overall, this work highlights a promising approach for converting mining waste into efficient, low-cost sorbents, contributing to sustainable heavy metal remediation and waste valorization efforts.

Keywords: Mining waste valorization; Thermal modification; Heavy metal removal; Copper adsorption; Waste-derived sorbents.
Received: 18 July 2025; Revised: 20 September 2025; Accepted: 30 September 2025
Article type: Research article.

1. Introduction

The growing body of research on oil pollution reflects its increasing recognition as a serious global environmental concern and highlights the urgent need for effective remediation technologies. In parallel, contamination of soil and water by heavy metals remains a pressing environmental challenge, especially in regions with intensive mining and metallurgical activities. Toxic metal ions such as copper (Cu^{2+}), cadmium (Cd^{2+}), and nickel (Ni^{2+}) are of particular concern due to their persistence, non-biodegradability, and ability to bioaccumulate in living organisms. Even at trace levels, these metals can pose serious risks to both ecological systems and human health.[1,2] The development of efficient, low-cost, and sustainable methods for heavy metal removal from wastewater is thus a critical area of research. Among various remediation techniques, adsorption is recognized for its simplicity, cost-effectiveness, and ability to achieve high removal efficiencies.[3] However, the application of commercial adsorbents like activated carbon is often limited by high production and regeneration costs.[4] Consequently, researchers have increasingly explored natural minerals and waste materials as alternative adsorbents.

The use of natural and synthetic zeolites is considered promising,[5–9] with the latter being produced by hydrothermal crystallization of alkaline aluminosilicate compositions in an aqueous medium under atmospheric or elevated pressure and at temperatures ranging from 120 – 200 °C. The reaction mixtures for zeolite synthesis include silicon and aluminum compounds, water, and alkaline and organic components. Depending on the structure and chemical composition of the zeolites, the molar ratio of SiO_2/Al_2O_3 can vary widely; the higher the SiO_2/Al_2O_3 ratio, the more active the zeolite.[6–10] The disadvantages of synthetic zeolite sorbents include their low mechanical strength and the use of pure inorganic and organic compounds in their synthesis, which increases production costs.

Alongside synthetic inorganic sorbents, natural minerals,

[1]*Department of Chemical Processes and Industrial Ecology, Mining and Metallurgical Institute named after O.A. Baikonurov, Satbayev University, 22 Satbaev street, Almaty, 050013, Kazakhstan*
[2]*Department of Environmental Engineering, Faculty of Chemical and System Engineering, University of Chemical Technology and Metallurgy, 8 Kliment Ohridski blvd., Sofia, 1756, Bulgaria*
[*]*Email:* a.kalymbet@satbayev.university (A. Kalymbet); s.kubekova@satbayev.university (S. Kubekova)

especially clay minerals, are widely used for removing heavy metal cations from water. Clays are among the most abundant and cost-effective natural sorbents available. Their layered aluminosilicate structure, combined with a high surface area, strong cation exchange capacity (CEC), and numerous functional groups, makes them particularly well-suited for binding metal ions in aqueous environments.[11] Montmorillonite, kaolinite, and illite are among the most studied clay minerals. Montmorillonite, for instance, can exhibit CEC values up to 150 meq/100 g, allowing effective removal of cationic species such as Cu^{2+}, Pb^{2+}, and Zn^{2+} through ion exchange and surface complexation mechanisms.[12] In addition to natural materials, industrial and agricultural wastes have gained attention as potential sorbents. For instance, modified rice husks,[13] fruit peels,[14] and biochars have been reported with promising adsorption capacities for various heavy metals. Similarly, natural zeolites and peat have been widely investigated.[15,16] Recently, activated carbon derived from biomass has also been studied as a sustainable adsorbent for metal ions, with promising structural and surface characteristics.[17]

A review of the literature on inorganic sorbents reveals that both natural and synthetic variants predominantly consist of silicon-, aluminum-, and phosphorus-based compounds. The synthesis of synthetic sorbents often involves complex, multi-step procedures and relies on discrete inorganic precursors as well as expensive organic reagents. To overcome these limitations, mining and ore beneficiation wastes, rich in aluminosilicate minerals, offer a promising and underutilized alternative feedstock for the production of inorganic sorbent materials. Despite its substantial mineral resources, Kazakhstan is confronted with serious environmental issues related to the accumulation of mining and metallurgical waste. Recent assessments estimate that more than 26 billion tonnes of solid waste have accumulated nationwide, with approximately 15 billion tonnes attributed to the mining and metallurgical industries. This includes over 5 billion tonnes of waste from non-ferrous metallurgy (such as copper, aluminum, lead-zinc, and gold) and more than 6 billion tonnes from ferrous metallurgy. Additionally, around 1 billion tonnes of industrial waste are generated annually, primarily comprising overburden, beneficiation tailings, slags, and other technogenic by-products.[18] These wastes, owing to their composition and abundance, offer an underutilized resource for the development of phosphate-modified sorbents capable of binding metal ions via precipitation, complexation, and ion exchange mechanisms.[19,20]

Recent studies have explored various modified phosphate-based sorbents for heavy metal removal from aqueous solutions, including iron phosphates, bio-waste composites, and thermally activated materials.[21–26] However, few works have focused on the valorization of gold mining waste specifically for synthesizing Cu^{2+}-selective silicophosphate sorbents via combined acid and thermal treatment. The present study advances this direction by employing minimally processed gravity tailings and evaluating both equilibrium and dynamic sorption behavior under relevant conditions. Although previous studies have demonstrated the potential for producing effective sorbent materials from gold ore beneficiation waste through acid pretreatment and thermal processing, as well as the enhancement of sorbent performance via phosphoric acid activation, the combined effects of orthophosphoric acid concentration, calcination temperature, and initial mineralogical composition on the sorption behavior of such materials remain insufficiently investigated.[27–29]

This study contributes to that effort by investigating the thermal treatment of oil-contaminated soils and analyzing the characteristics of the recovered oil products. Specifically, we focused on the Karazhanbas oil field, where we applied thermal treatment to contaminated soil to evaluate both the efficiency of the cleaning process and the properties of the resulting liquid extract. This study aims to develop and comprehensively characterize phosphate-modified sorbents synthesized from tailings of the gold-bearing Akbakay deposit. The influence of phosphoric acid concentration and thermal treatment parameters on the structural evolution, surface physicochemical properties, and Cu^{2+} adsorption performance of the resulting materials was systematically investigated. The overarching goal is to evaluate the potential of these waste-derived sorbents for efficient and sustainable application in heavy metal removal from contaminated aqueous systems.

2. Materials and Methods

2.1 Raw Materials and Sorbent Preparation

Phosphate-modified sorbents were synthesized from tailings of the gold-bearing Akbakay deposit (Kazakhstan). The waste material was first ground to a particle size of 0–10 μm using wet milling, followed by drying at 105 °C for 1 h. Thermal–acid treatment was conducted using orthophosphoric acid (H_3PO_4) at two concentrations (20 wt.% and 35 wt.%), with subsequent calcination at three temperatures: 400, 600, and 800 °C. Acid dosage was calculated based on the content of acid-reactive components in the raw material.

The resulting six samples were designated as follows:

- **Sample 1**: 400 °C, 20 wt.% H_3PO_4
- **Sample 2:** 400 °C, 35 wt.% H_3PO_4
- **Sample 3:** 600 °C, 20 wt.% H_3PO_4
- **Sample 4:** 600 °C, 35 wt.% H_3PO_4
- **Sample 5:** 800 °C, 20 wt.% H_3PO_4
- **Sample 6:** 800 °C, 35 wt.% H_3PO_4

2.2 Characterization Techniques

X-ray diffraction (XRD) analysis was carried out on a DRON-3 diffractometer equipped with CuKα radiation (β-filter) operating at 35 kV and 20 mA (θ–2θ scan mode, 2°/min). Phase identification was performed using the ICDD PDF2 database, and semi-quantitative analysis was conducted using the equal-hinge-plate method. Elemental composition was

determined by electron probe microanalysis (EPMA) using a JEOL–733 instrument equipped with an X-ray microanalyzer. Surface morphology was analyzed using scanning electron microscopy (SEM; Jeol JSM-6490LA). Specific surface area and pore characteristics were measured by N_2 adsorption–desorption isotherms using a Beishide BSD-660 instrument. Zeta potential measurements were performed using a Zetasizer Nano ZS90 (Malvern Instruments) to evaluate surface charge behavior. Fourier transform infrared (FTIR) spectroscopy was performed using a Bruker Alpha-II ATR-FTIR spectrometer to assess functional groups and phosphate incorporation. Batch sorption experiments were conducted to evaluate Cu^{2+} uptake. A 3.0 g sample of each sorbent was mixed with 100 mL of Cu^{2+} solution at varying initial concentrations (1, 10, 20, 30, and 40 mg/L). The suspensions were stirred at 200 rpm for 24 h at room temperature. After filtration (0.45 μm), the residual Cu^{2+} concentration was measured using an AA-7000 atomic absorption spectrometer (Shimadzu). Sorption capacity (q_e, mg/g) was calculated based on the difference between initial and final concentrations. Kinetic studies were carried out using a 10 mg/L Cu^{2+} solution (250 mL) and 3.0 g of sorbent. The suspensions were agitated at 200 rpm, and samples were withdrawn at predetermined time intervals (2, 5, 10, 30, 60, and 120 min), filtered (0.45 μm), and analyzed for residual Cu^{2+} by AAS. Dynamic sorption performance was assessed using a fixed-bed glass column (10 cm height, 10 mm internal diameter) packed with 3.0 g of sorbent. Prior to the experiment, the column was flushed with 50 mL of distilled water at a flow rate of 2 mL/min using a peristaltic pump. A Cu^{2+} solution (10 mg/L) was continuously passed through the column under the same flow conditions. Effluent was collected in six 50 mL fractions (totaling 300 mL), and Cu^{2+} concentration in each fraction was determined by AAS to assess breakthrough behavior and dynamic capacity.

3. Results and discussion

3.1 Analysis of Composition and Structure of Materials

The structural evolution of the phosphate-modified sorbents synthesized from Akbakay gold ore waste was systematically investigated using X-ray diffraction (XRD), with the results summarized in Table 1 and Fig. 1 (see *Supporting Information*

Table 1: Results of semi-quantitative analysis of crystalline phases by XRD.

Name	Formula	Mineral	Concentration, wt.%
Initial waste	SiO_2	Quartz	67
	$(Na_{0.84}Ca_{0.16})Al_{1.16}Si_{2.84}O_8$	Albite	12
	$Fe_{2.95}(PO_4)_2(OH)_2$	Lipscombite	7
	$K_{0.932}Al_2(Al_{0.932}Si_{3.068}O_{10})(OH)_{1.744}F_{0.256})$	Mica (muscovite)	3
	$CaMg(CO_3)_2$	Dolomite	11
Sample 1	SiO_2	Quartz	70
	$(Na_{0.98}Ca_{0.02})(Al_{1.02}Si_{2.98}O_8)$	Albite	12
	$CaMg(CO_3)_2$	Dolomite	12
	$Fe_{2.95}(PO_4)_2(OH)_2$	Lipscombite	6
Sample 2	$(Na_{0.98}Ca_{0.02})(Al_{1.02}Si_{2.98}O_8)$	Albite	10
	SiO_2	Quartz	63
	$(K_{0.94}Na_{0.03})(Al_{1.67}Mg_{0.04}Fe_{0.34})(Si_{3.26}Al_{0.74})O_{10}$ $(OH)_{0.94}F_{0.06})_2$	Mica	5
	$CaMg(CO_3)_2$	Dolomite	11
	$Fe_{2.95}(PO_4)_2(OH)_2$	Lipscombite	10
Sample 3	SiO_2	Quartz	68
	$Na(AlSi_3O_8)$	Albite	11
	$Ca(Mg,Fe)(CO_3)_2$	Dolomite	20
	$(K_{0.92}Na_{0.08})(Al_{1.86}Fe_{0.07}Mg_{0.07}Ti_{0.02})(Si_{3.03}Al_{0.97})O_{10}(OH)_2$	Mica	1
Sample 4	SiO_2	Quartz	76
	$(Na_{0.98}Ca_{0.02})(Al_{1.02}Si_{2.98}O_8)$	Albite	8
	$Ca(Mg,Fe)(CO_3)_2$	Dolomite	7
	$(K_{0.92}Na_{0.08})(Al_{1.86}Fe_{0.07}Mg_{0.07}Ti_{0.02})(Si_{3.03}Al_{0.97})O_{10}(OH)_2$	Mica	4
	$Fe_{2.95}(PO_4)_2(OH)_2$	Lipscombite	5
Sample 5	SiO_2	Quartz	80
	$Na(AlSi_3O_8)$	Albite	12
	$(K_{0.92}Na_{0.08})(Al_{1.86}Fe_{0.07}Mg_{0.07}Ti_{0.02})(Si_{3.03}Al_{0.97})O_{10}(OH)_2$	Mica	5
	$Fe_{2.95}(PO_4)_2(OH)_2$	Lipscombite	3
Sample 6	SiO_2	Quartz	72
	$Na(AlSi_3O_8)$	Albite	12
	$Fe_{2.95}(PO_4)_2(OH)_2$	Lipscombite	5
	$(K_{0.92}Na_{0.08})(Al_{1.86}Fe_{0.07}Mg_{0.07}Ti_{0.02})(Si_{3.03}Al_{0.97})O_{10}(OH)_2$	Mica	11

file Fig. S1). The initial waste material was composed primarily of quartz (67 wt.%), along with albite (12 wt.%), dolomite (11 wt.%), lipscombite (7 wt.%), and muscovite mica (3 wt.%), reflecting a mineralogically diverse mixture of silicate, carbonate, and phosphate phases. Upon phosphoric acid treatment and thermal activation, significant changes in phase composition were observed. Quartz remained the dominant phase across all samples and exhibited an increasing trend with calcination temperature. The highest quartz content (80 wt.%) was found in Sample 5 (800 °C, 20 wt.% H_3PO_4), indicating the progressive enrichment of thermally stable silica as less stable phases decomposed or transformed at elevated temperatures. Albite was consistently present in all synthesized samples, ranging from 8–12 wt.%, suggesting its structural stability under both acidic and thermal conditions. Dolomite showed a more variable trend: its concentration increased notably in Sample 3 (20 wt.%), synthesized at 600 °C with 20 wt.% H_3PO_4, but decreased significantly in Sample 4 (7 wt.%) and was undetectable in Sample 5. This suggests partial thermal decomposition or transformation of carbonates under higher temperature regimes, in line with known thermal behavior of dolomitic phases.

Mica phases exhibited sample-specific variability. While present at low levels in most samples, mica content reached 11 wt.% in Sample 6 (800 °C, 35 wt.% H_3PO_4). This spike is likely due to recrystallization or the formation of new mica-like phases under high phosphate loading and elevated temperatures, potentially stabilized by interactions with residual silicates and aluminates. One of the most critical observations was the behavior of lipscombite ($Fe_{2.95}(PO_4)_2(OH)_2$), a key iron phosphate phase. Its highest concentration (10 wt.%) was detected in Sample 2 (400 °C, 35 wt.% H_3PO_4), confirming that moderate thermal treatment combined with high phosphate availability favors the stabilization of this phase. This is consistent with earlier studies reporting the formation of lipscombite under similar phosphate-rich, low-to-moderate temperature conditions. However, its content diminished with increasing calcination temperature, indicating that lipscombite undergoes dehydroxylation and subsequent transformation into more thermally stable, possibly amorphous Fe/Al-phosphate or silicophosphate phases at 600–800 °C. Interestingly, the presence of lipscombite was not directly correlated with sorption performance. For example, Sample 3 (600 °C, 20 wt.% H_3PO_4) exhibited superior Cu^{2+} adsorption capacity despite containing only 1 wt.% mica and no significant enhancement in lipscombite content. In contrast, Sample 4, synthesized under similar thermal conditions but with higher acid loading (35 wt.%), showed reduced adsorption performance. This decline can be attributed to over-phosphatization, which likely led to pore blockage and reduced availability of active Fe/Al surface sites, as further supported by SEM and BET analyses discussed in Section 3.2.

Overall, the XRD results clearly demonstrate that both phosphoric acid concentration and calcination temperature exert a profound influence on the phase composition of the synthesized sorbents (see *Supporting Information file* Fig. S1). Quartz enrichment, dolomite decomposition, mica evolution, and phosphate phase dynamics collectively contribute to shaping the structural framework of the materials, which in turn governs their surface functionality and sorption efficiency.

3.1.1 EPMA

Electron Probe Microanalysis (EPMA) was used to determine the changes in chemical composition of the materials depending on the synthesis conditions. Table 2 presents the mass fractions of oxides identified in the initial waste and in the modified samples. The initial material is characterized by a high content of silicon dioxide ($SiO_2 \approx 67$ wt.%), alumina ($Al_2O_3 \approx 13$ wt.%), and alkali components such as Na_2O (4.72 wt.%) and K_2O (2.65 wt.%). Minor amounts of P_2O5, SO_3, CaO, TiO_2, and FeO are also present, reflecting the mixed mineral composition of the raw waste. Modification with phosphoric acid and subsequent thermal treatment leads to noticeable compositional changes. In particular, an increase in P_2O_5 content is observed across all treated samples, indicating successful incorporation of phosphate groups into the structure. The highest P_2O_5 content (7.79 wt.%) was detected in Sample 2, synthesized at 400 °C with 35 wt.% acid,

Table 2: Results of Material composition of crystalline phases by EPMA. All results in compounds are expressed in mass fractions, %.

Spectrum	Na_2O	MgO	Al_2O_3	SiO_2	P_2O_5	SO_3	K_2O	CaO	TiO_2	MnO	FeO	BaO	Total
Initial waste	4.72	1.93	12.92	66.99	0.75	0.76	2.65	3.35	0.58	0.18	5.12	0.05	100.00
Sample 1	4.61	1.75	12.89	65.94	4.36	0.71	2.44	2.81	0.60	nf[1]	3.75	0.13	100.00
Sample 2	4.62	1.68	12.18	62.07	7.79	0.85	2.28	3.60	0.53	nf	4.17	0.22	100.00
Sample 3	4.70	1.97	13.06	64.47	4.78	nf	2.52	3.48	0.71	0.16	4.09	0.07	100.00
Sample 4	2.06	1.90	13.90	64.15	5.91	nf	4.69	2.94	0.61	0.16	3.67	nf	100.00
Sample 5	4.30	2.50	12.08	59.98	5.82	0.77	2.55	5.09	0.54	0.30	6.03	0.04	100.00
Sample 6	4.24	2.78	11.90	58.06	7.51	0.70	2.77	4.68	0.40	0.30	6.45	0.21	100.00

[1] nf=not found.

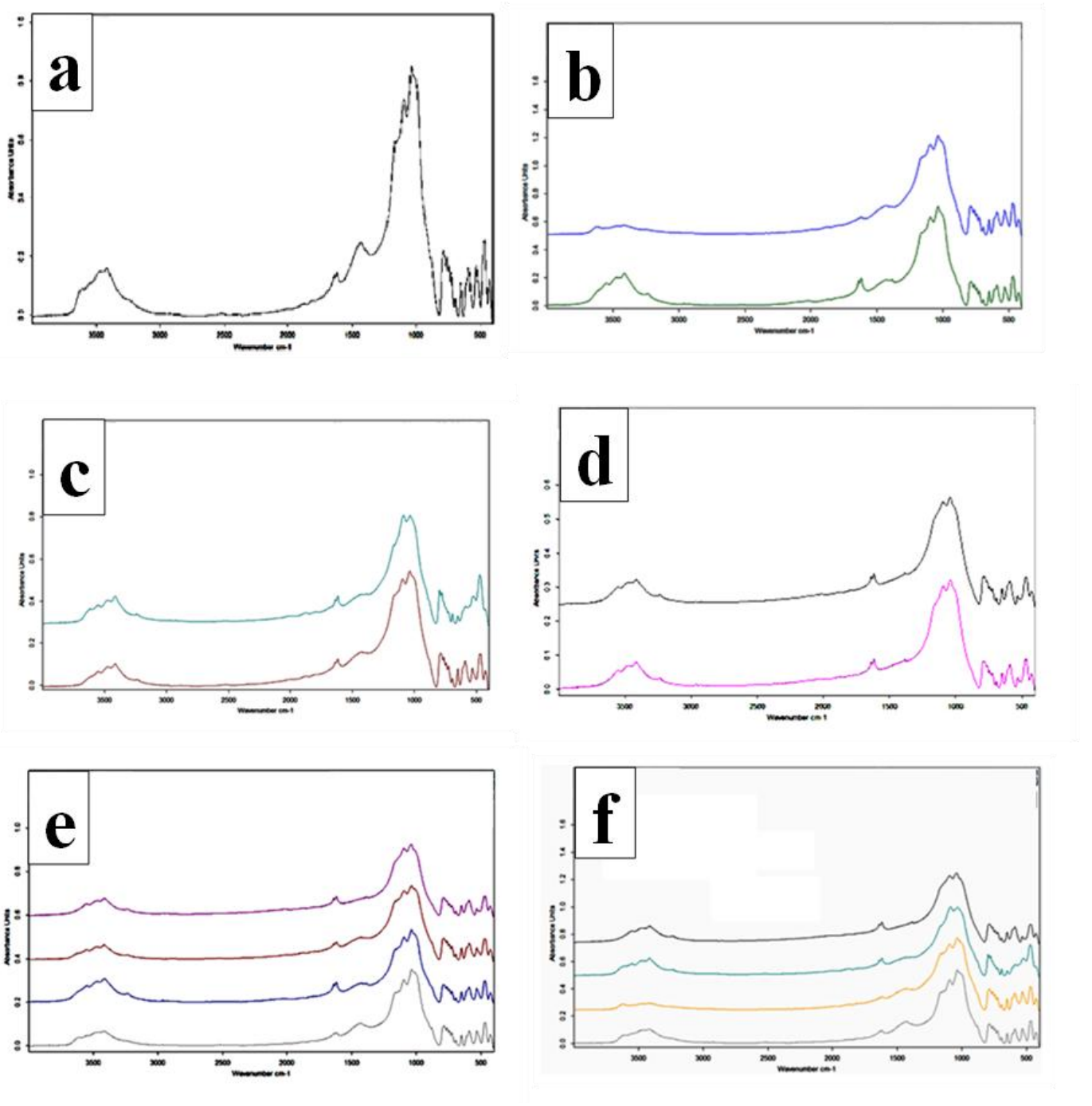


Fig. 1: FTIR spectroscopy of samples: (a) Initial waste; (b) comparison of sample 1 (green) and sample 2 (blue); (c) comparison of sample 3 (red) and sample 4 (light green); (d) comparison of sample 5 (purple) and sample 6 (black); (e) comparison of initial waste (gray), sample 1 (blue), sample 3 (red) and sample 5 (purple); (f) comparison of initial waste (gray), sample 2 (yellow), sample 4 (light green) and sample 6 (black).

suggesting more efficient phosphate binding under these conditions. At higher temperatures (600–800 °C), a general trend of decreasing SiO_2 and Al_2O_3 contents is observed, especially in Sample 6, which also shows elevated levels of FeO (6.45 wt.%) and P_2O_5 (7.51 wt.%). This may indicate partial transformation of aluminosilicates and enhanced concentration of iron phosphate phases such as lipscombite. The presence and variation of CaO, MgO, and K_2O among the samples further reflect the redistribution of components due to the acid treatment and heat exposure. Overall, the chemical composition data confirm that both the acid concentration and calcination temperature significantly influence the phase composition and elemental distribution in the resulting materials.

3.1.2 FTIR Spectroscopy

The FTIR spectra of the initial material and synthesized samples are presented in Fig. 1. The spectral features allow for

the identification of key functional groups and structural transformations occurring during acid modification and thermal treatment. The spectrum of the initial waste (Fig. 1a) exhibits characteristic bands associated with silicate minerals. A broad absorption band centered around 3400 cm^{-1} corresponds to O–H stretching vibrations from adsorbed water and hydroxyl groups. The band at approximately 1630 cm-1 is attributed to H–O–H bending vibrations of molecular water. Strong absorption in the range of 1000–1100 cm^{-1} is due to Si–O–Si asymmetric stretching vibrations, typical of quartz and aluminosilicate phases. Bands near 790 and 470 cm^{-1} are assigned to Si–O symmetric stretching and bending modes, respectively. A comparison of Samples 1 and 2 (Fig. 1b), both treated at 400 °C but with different acid concentrations (20 wt.% and 35 wt.%, respectively), shows subtle differences in band intensity and position. In Sample 2, the band associated with P–O stretching vibrations (~1050 cm^{-1}) becomes more pronounced, indicating the incorporation of phosphate groups into the structure, likely through the formation of iron phosphate phases such as lipscombite.

Similarly, in Fig. 1c, comparing Samples 3 and 4 (synthesized at 600 °C) reveals a decrease in hydroxyl-related absorption bands and a slight shift in Si–O–Si bands, suggesting increased condensation of the silicate network and dehydration processes. The presence of phosphate bands remains evident, especially in Sample 4 (35 wt.% acid), confirming the role of acid concentration in promoting phosphate phase formation. The spectra of high-temperature samples (Samples 5 and 6, Fig. 1d) show a further reduction in hydroxyl-related bands, consistent with advanced dehydroxylation and thermal stabilization of the structure. The P–O band remains visible in Sample 6, indicating the retention of phosphate species even after calcination at 800 °C.

Fig. 1e and 1f summarize spectral trends across samples synthesized with both acid concentrations and varying temperatures. In both series, a gradual sharpening and shift of Si–O–Si bands is observed with increasing temperature, suggesting improved crystallinity and structural ordering. The appearance and intensification of phosphate bands in acid-modified samples, particularly those treated with 35 wt.% H_3PO_4, confirm successful incorporation of phosphate units into the solid matrix. Overall, the FTIR data support the conclusions drawn from XRD and EPMA analyses: phosphoric acid treatment induces the formation of phosphate-containing phases, while increasing calcination temperature leads to structural dehydration and enhanced silicate framework ordering.

3.2 Surface Properties of Materials

Scanning Electron Microscopy (SEM) was employed to examine the surface morphology and microstructural evolution of the raw gold ore waste and phosphate-modified sorbents under varying synthesis conditions. Representative SEM micrographs at a magnification of 1000× are shown in Fig. 2 (a–g). The SEM image of the untreated waste material (Fig. 2a) displays a dense and compact surface, with angular particles and limited porosity. The particle boundaries appear irregular, and no clear pore networks or textural features are observed, suggesting a low surface area and minimal accessibility for sorption interactions. Upon phosphoric acid modification and thermal treatment, substantial morphological transformations were evident. Samples 1 and 2 (Fig. 2b and 2c), synthesized at 400 °C with 20 wt.% and 35 wt.% H_3PO_4 respectively, exhibit the onset of surface etching, characterized by the appearance of fissures, cracks, and surface roughening. These features indicate partial dissolution and leaching of mineral phases during acid treatment, leading to the formation of loosely aggregated, more friable structures. The increased surface irregularity may contribute to a moderate enhancement in surface reactivity.

Further thermal activation at 600 °C led to more pronounced structural rearrangements. Sample 3 (Fig. 2d, 20 wt.% acid) demonstrates fragmented, granular structures with signs of developing pore channels and microcavities—evidence of acid-promoted mineral decomposition combined with thermal dehydration. In contrast, Sample 4 (Fig. 2e, 35 wt.% acid) exhibits a highly disrupted morphology with extensive fragmentation and rough, porous clusters. These observations suggest that a synergistic effect of higher acid concentration and moderate calcination enhances matrix disintegration and porosity development, which is favorable for sorbent performance. At the highest calcination temperature (800 °C), Samples 5 and 6 (Fig. 2f and 2g) exhibit morphologies indicative of advanced thermal restructuring. Sample 5 shows evidence of sintering and partial particle fusion, leading to the loss of discrete particle boundaries and reduction in textural contrast. Sample 6, synthesized with 35 wt.% H_3PO_4, displays even more extensive structural modification, with the formation of irregular porous clusters and partially melted surfaces. These features point to the onset of vitrification or the formation of amorphous phosphate/silicate-rich glassy phases, commonly reported under high-temperature acid-thermal processing.

In summary, SEM analysis clearly illustrates that both acid concentration and calcination temperature are key factors governing the morphological evolution of the synthesized materials. Lower temperatures favor surface activation through etching and cracking, while intermediate temperatures promote pore formation and particle disaggregation. Excessive thermal input at 800 °C induces sintering and partial melting, potentially reducing accessible surface area. These morphological trends are consistent with BET and sorption data (Sections 3.3 and 3.4), highlighting the importance of tuning synthesis parameters to optimize surface properties and sorption performance.

3.2.1 Zeta Potential Analysis

The zeta potential values of the raw and phosphate-modified samples are summarized and presented in *Supporting Information file* Fig. S2, which illustrates the impact of acid

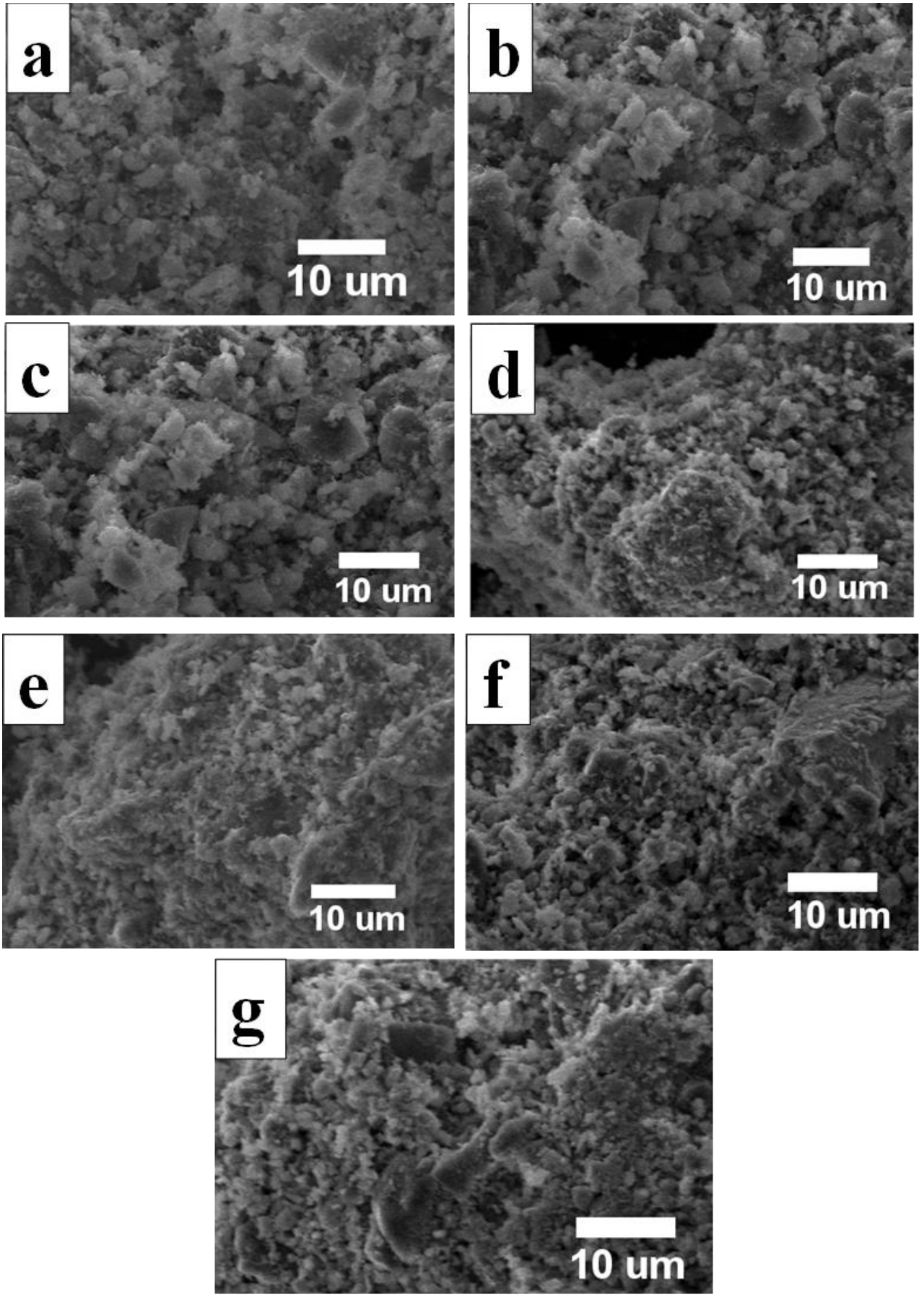


Fig. 2: SEM images of samples at 1000 magnification: (a) Initial waste; (b) sample 1; (c) sample 2; (d) sample 3; (e) sample 4; (f) sample 5; (g) sample 6.

concentration and thermal treatment on surface charge characteristics. The initial gold ore waste exhibited a zeta potential of –10.4 mV, indicative of limited surface activation and a relatively low electrostatic repulsion capacity. Following modification, all treated samples showed significantly more negative zeta potential values, ranging from –14.1 mV to –20.1 mV. This shift reflects an overall increase in surface negativity, attributed to the incorporation of phosphate groups and structural reorganization during acid and thermal treatment. Among the modified samples, Sample 3 (600 °C, 20 wt.% H_3PO_4) exhibited the most negative zeta potential (–20.1 mV) (*Supporting Information file* Fig. S2 (b)), suggesting the highest degree of surface functionalization and enhanced colloidal stability. This pronounced shift supports the presence of abundant anionic surface sites, likely due to phosphate coordination on Fe/Al-rich domains. Samples 1 and 2 (400 °C, 20 and 35 wt.% acid) also displayed substantially enhanced surface charges, with zeta potentials of –18.0 mV and –16.3 mV, respectively, which presented in *Supporting Information file* Fig. S2 (a). These results indicate effective acid-induced surface modification at lower calcination temperatures. In contrast, Samples 5 and 6, treated at 800 °C, showed comparatively moderate zeta potentials (–14.1 mV and –14.8 mV) that shown in *Supporting Information file* Fig. S2 (c), likely due to partial sintering or surface densification that limits the exposure of active sites. Sample 4 (600 °C, 35 wt.% acid) showed an intermediate value (–16.1 mV) (*Supporting Information file* Fig. S2 (b)), suggesting that excess acid loading may reduce surface charge by blocking or neutralizing active sorption sites.

The data from *Supporting Information file* Fig. S2 (d–e), comparing groups of samples and the raw material, reinforce the trend of increasingly negative zeta potentials with appropriate acid–thermal treatment combinations. This enhancement in surface charge is particularly relevant for aqueous-phase sorption applications, as more negative zeta potentials favor stronger electrostatic attraction toward positively charged metal ions, such as Cu^{2+}. These findings are in line with prior reports on phosphate-functionalized mineral-based sorbents, which have demonstrated similar zeta potential trends and improved adsorption behavior.[31] In conclusion, the zeta potential results confirm that phosphoric acid treatment combined with controlled thermal activation effectively enhances the surface charge characteristics of the synthesized sorbents. The extent of modification is strongly influenced by the acid concentration and calcination temperature, both of which must be optimized to maximize sorption potential through electrostatic interactions.

3.2.2 Surface area and porosity analysis

The surface characteristics of the initial waste material and synthesized sorbents were assessed using nitrogen adsorption–desorption isotherms, with the results summarized in Table 3. The data include Brunauer–Emmett–Teller (BET) surface area, Langmuir surface area, micropore area (Dubinin–Radushkevich (D-R) model), total pore volume, average pore diameter, and BJH (Barrett–Joyner–Halenda) parameters. The unmodified initial waste displayed the highest BET surface area of 6.02 m^2/g, which decreased in all modified samples regardless of the synthesis temperature or acid concentration. This reduction is likely attributed to partial collapse or densification of the pore structure during acid treatment and thermal processing. Among the modified samples, Sample 3 (600 °C, 20 wt.% H3PO4) showed a relatively moderate BET surface area (4.02 m^2/g), whereas the lowest value was recorded for Sample 2 (400 °C, 35 wt.% H_3PO_4), at 2.19 m^2/g. A similar trend was observed in the Langmuir surface areas, with values ranging from 9.58 m^2/g for the raw material to 3.52 m^2/g for Sample 2. The D-R micropore areas followed a slightly different pattern, remaining relatively stable across modified samples (2.8–3.6 m^2/g), indicating the preservation of some microporosity even after modification. Total pore volumes were highest in the initial waste (0.0191 cm^3/g), and slightly lower in the modified materials, with Sample

Table 3: Textural Properties of Unmodified and Modified Sorbents.

Parameter	Initial waste	Sample 1	Sample 2	Sample 3	Sample 4	Sample 5	Sample 6
BET Surface Area (m^2/g)	6.02	3.86	2.19	4.02	2.79	3.09	2.71
Langmuir Surface Area (m^2/g)	9.58	6.46	3.52	6.48	4.46	5.01	4.37
D-R Micropore Area (m^2/g)	6.46	3.56	3.48	3.20	3.05	3.23	2.82
Total Pore Volume (cm^3/g)	0.0191	0.0141	0.0103	0.0145	0.0106	0.0163	0.0172
Average Pore Diameter (nm)	12.69	14.61	18.83	14.38	15.18	21.08	25.38
BJH Desorption Area (m^2/g)	6.70	4.51	2.23	4.57	3.10	3.78	3.11
BJH Pore Volume (cm^3/g)	0.0186	0.0136	0.0101	0.0143	0.0104	0.0160	0.0171

6(800 °C, 35 wt.% H_3PO_4) showing a relatively high value (0.0172 cm^3/g), suggesting the development of mesoporosity at elevated temperatures.

Surface area and porosity analysis revealed trends distinct from conventional acid-activated adsorbents. While typical phosphoric acid treatment increases the surface area of clays,[30] the BET surface area of the silica-rich waste material decreased after modification (from 6.02 m^2/g to 2.19–4.02 m^2/g), likely due to partial pore collapse and thermal densification. Nevertheless, the average pore diameter increased in most modified samples, particularly those thermally treated, indicating the development of mesoporosity. Sample 6 (800 °C, 35 wt.% H_3PO_4) exhibited the largest average pore diameter (25.38 nm), with BJH desorption data further confirming the mesoporous character. This structural transformation likely improves active site accessibility and compensates for the reduced surface area, a behavior consistent with previous observations in waste-derived adsorbents.[31] Overall, the surface textural data indicate that acid modification followed by thermal treatment leads to a reduction in surface area but promotes mesopore development. These transformations are more pronounced at higher acid concentrations and elevated calcination temperatures, potentially enhancing the accessibility of active sites for sorption processes despite the reduction in overall surface area.

3.3 Equilibrium and Kinetics of the Sorption Process of Copper Cations

The sorbent synthesized at 600 °C using 20 wt.% phosphoric acid (Sample 3) exhibited optimal physicochemical characteristics, including improved surface accessibility and more uniform pore distribution. These properties contributed to its significant sorption performance, which was evaluated under both static (batch) and dynamic (fixed-bed column) conditions.

3.3.1 Equilibrium Sorption Studies

Batch adsorption experiments were carried out using Sample 3 to evaluate its equilibrium adsorption capacity (q_e) and Cu^{2+} removal efficiency (RE). The initial Cu^{2+} concentrations (C_0) ranged from 1 to 40 mg/L. For each experiment, 3.0 g of the sorbent was added to 100 mL of the metal ion solution. The initial pH of the solutions was adjusted to 4.5–6.0, simulating conditions typical for $CuSO_4 \cdot 5H_2O$ solutions without external buffering. After reaching equilibrium, the residual Cu^{2+} concentrations (C_e) were measured, and the results are summarized in *Supporting Information file* Table S1. Under equilibrium conditions, Sample 3 demonstrated consistently high Cu^{2+} removal efficiency (RE) across the tested concentration range (1–40 mg/L), with removal percentages exceeding 97%. The experimental adsorption capacity (q_e) increased with increasing initial Cu^{2+} concentration (C_0), reaching a maximum of 1.33 mg/g at 40 mg/L.

The experimental data were fitted using four isotherm models (Fig. 3): Freundlich, Langmuir, Sips, and Dubinin–Radushkevich (D–R). Among these, the D–R and Langmuir models showed the best agreement with the experimental data, with calculated values closely matching observed q_e values across all concentrations. The Sips model also provided a reasonable fit, whereas the Freundlich model tended to underestimate the adsorption capacity at higher concentrations. These results suggest that Cu^{2+} adsorption onto Sample 3 is most likely monolayer and occurs on a homogeneous surface.

The fitted parameters and statistical indicators for the applied isotherm models are summarized in *Supporting Information file* Table S2. Among the four tested models, the Dubinin–Radushkevich (D–R) model provided the best overall fit to the experimental data, with the highest coefficient of determination (R^2 = 0.930) and the lowest error metrics (SSE = 0.079, RMSE = 0.163). This result suggests that the adsorption process is primarily physical in nature and that

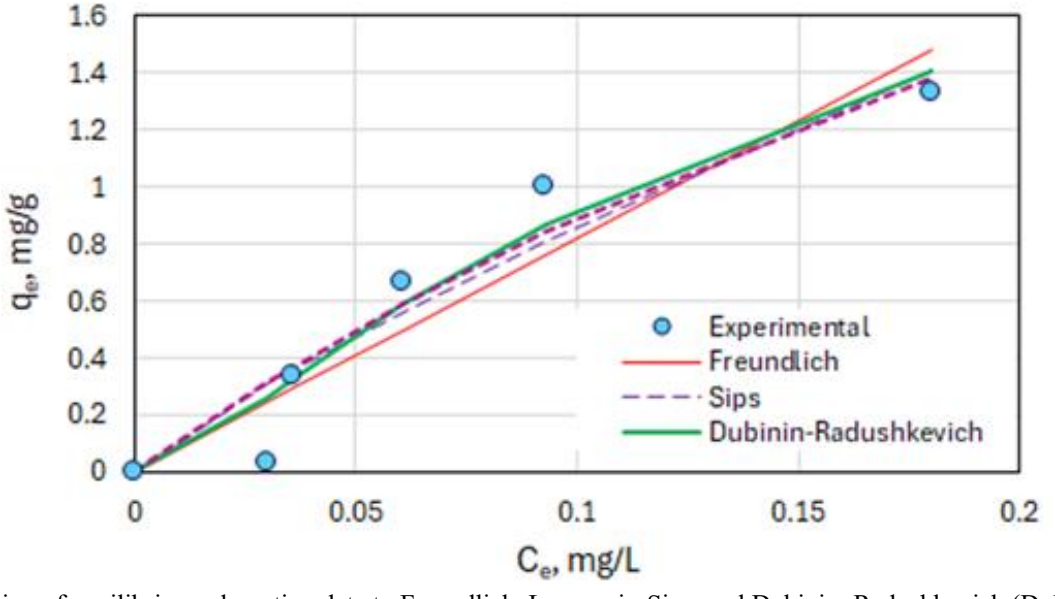


Fig. 3: Fitting of equilibrium adsorption data to Freundlich, Langmuir, Sips, and Dubinin–Radushkevich (D–R) models.

pore-filling plays a significant role. The Langmuir model also showed strong correlation (R^2 = 0.909), supporting the assumption of monolayer adsorption on a homogeneous surface. The maximum monolayer adsorption capacity predicted by this model was 4.37 mg/g, which is in good agreement with the experimental trend. The Sips model, combining features of both Langmuir and Freundlich models, exhibited a moderate fit (R^2 = 0.882), with predicted parameters q_m = 6.07 mg/g and n_S = 0.85, indicating a slightly heterogeneous surface. Although the Freundlich model is typically used for heterogeneous surfaces, it showed the weakest fit here, with an unrealistic negative value of the Freundlich constant KF and the lowest R^2 value (0.860), likely due to its limited applicability at higher concentrations.

Overall, the results suggest that while the Langmuir and D–R models effectively describe the equilibrium behavior of Cu^{2+} adsorption onto Sample 3, the D–R model yields slightly better statistical consistency and may better reflect the adsorption mechanism under the studied conditions. While the Langmuir model reflects surface site saturation, the better fit of the D–R model indicates that pore filling dominates, consistent with physisorption in a heterogeneous structure.

3.3.2 Sorption Kinetics

Kinetic experiments were conducted to assess the rate and mechanism of Cu^{2+} ion sorption at an initial concentration (C_0) of 10 mg/L. Batch experiments were carried out using 3 g of sorbent in 250 mL of Cu^{2+} solution under constant agitation at 200 rpm. At predetermined time (t) intervals (2, 5, 10, 30, 60, and 120 minutes), aliquots were withdrawn, filtered through 0.45 µm membranes, and analyzed by atomic absorption spectroscopy (AAS) to determine the residual Cu^{2+} concentrations (C_t). The experimental data are summarized in *Supporting Information file* Table S3. Rapid uptake was observed within the first few minutes, indicating a strong initial affinity of the sorbent for Cu^{2+} ions. Equilibrium was gradually approached over time, with >99% removal achieved by 120 minutes. The kinetic experimental data were analyzed using pseudo-first-order, pseudo-second-order, intraparticle diffusion, and mixed order models (Fig. 4).

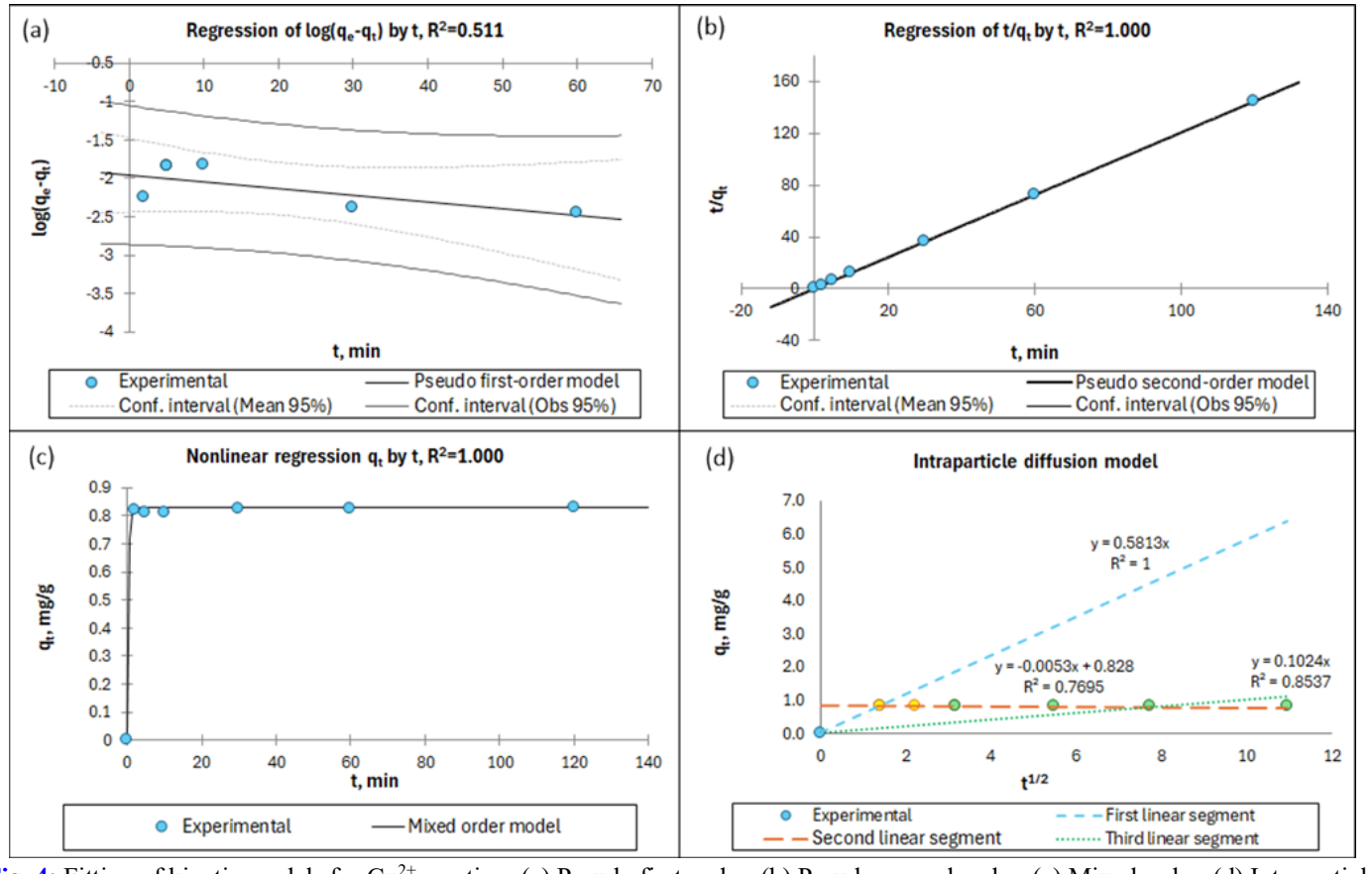


Fig. 4: Fitting of kinetic models for Cu^{2+} sorption: (a) Pseudo first-order; (b) Pseudo second-order; (c) Mixed order; (d) Intraparticle diffusion.

The values of the calculated kinetic parameters and error functions are presented in Table 4. The pseudo-first-order model is not proper. The good agreement between the pseudo-second-order model and the experimental data indicates that copper ions were adsorbed onto the Sample 3 surface primarily through chemisorption.

When the sorption process is governed by multiple mechanisms, the plot of qt versus $t^{1/2}$ typically exhibits a multi-linear profile. The first linear segment corresponds to external surface adsorption or boundary layer diffusion. The second linear segment reflects the gradual adsorption stage controlled by intraparticle diffusion within the pores of the sorbent.

Table 4: Values of the kinetic model parameters and error functions for the system Copper ions – Sample 3.

Model type	Model parameter			Error function		
Pseudo-first-order	k_1	q_{e1}		R_1^2	MSE	RMSE
Linear expression $\log(q_e - q_t) = \log q_e - \frac{k_1}{2.303}t$	-8.825x10^{-3}	0.141		0.511	0.058	0.241
Pseudo second-order	k_2	q_{e2}		R_2^2	MSE	RMSE
Linear expression $\frac{t}{q_t} = \frac{1}{k_2 q_e^2} + \frac{1}{q_e}t$	1.199x10^{-1}	0.828		1.000	0.018	0.135
Intraparticle diffusion	k_{i1}	k_{i2}		R_{i1}^2	R_{i2}^2	
Non-linear form $q_t = k_i t^{0.5} + I$	-0.005	0.1024		0.769	0.102	
Mixed order	k_1	k_2	f_2	R^2	MSE	RMSE
Non-linear form $q = q_e\left(\frac{1-\exp(-k_1 t)}{1 - f_2 \exp(-k_1 t)}\right)$	2.054	2.182	0.438	1.000	0.000	0.010

Finally, the third plateau region indicates the approach to equilibrium, where the rate of intraparticle diffusion decreases significantly due to the diminishing concentration of adsorbate in the solution. The plots of the intraparticle diffusion model for copper ions sorption have three sections, which means that the intraparticle diffusion was not the only mechanism involved. The first stage is clearly controlled by external surface adsorption. The second and third stages show poor or unreliable fits, indicating that the intraparticle diffusion model does not fully explain the entire sorption process, especially in the later phases. The mixed-order kinetic model provided an excellent fit to the experimental adsorption data, with an R^2 value of 1.000 and minimal RMSE (0.010), indicating outstanding predictive capability. The estimated rate constants, k^1=2.054 and k^2=2.182, along with the second-order contribution fraction f^2=0.438, suggest that the adsorption of copper ions onto Sample 3 is governed by a combination of physisorption and chemisorption mechanisms. The mixed kinetic behavior confirms the complexity of the process, supporting the presence of multiple simultaneous rate-limiting steps.

3.3.3 Dynamic Sorption (Fixed-Bed Column)

Dynamic sorption experiments were conducted using a fixed-bed column setup to evaluate sorption performance under continuous flow conditions. A glass column (10 cm height × 10 mm inner diameter) was packed with 3 g of sorbent and pre-conditioned by passing 50 mL of distilled water through the bed at a flow rate of 2 mL/min using a peristaltic pump. Subsequently, a Cu^{2+} solution (10 mg/L) was continuously pumped through the column at the same flow rate. The effluent was collected in six successive 50 mL fractions (total volume: 300 mL), and residual Cu^{2+} concentrations in each fraction were determined using atomic absorption spectroscopy (AAS). The results are summarized in *Supporting Information file* Table S4 and presented graphically in *Supporting Information file* Fig. S3. Column experiments confirmed the practical applicability of Sample 3 under continuous flow conditions. The total amount of Cu^{2+} adsorbed during the test reached approximately 2.540 mg, corresponding to a dynamic sorption capacity of 0.847 mg/g. Although this value is lower than that obtained under batch conditions, it demonstrates efficient performance under dynamic conditions. Comparable

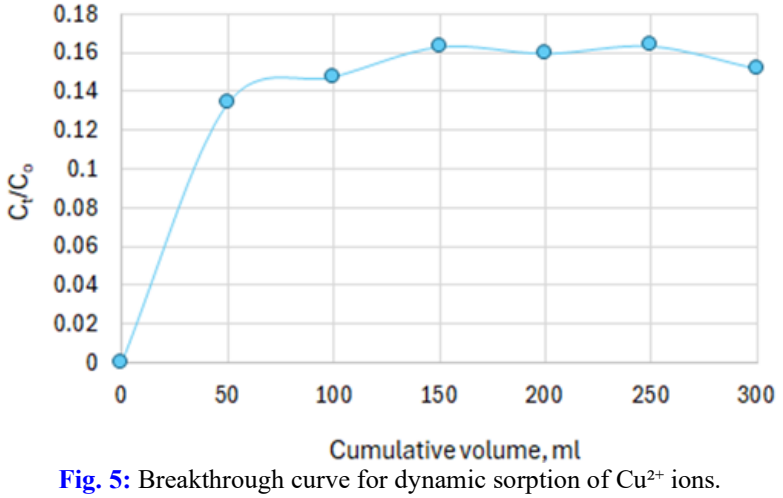


Fig. 5: Breakthrough curve for dynamic sorption of Cu^{2+} ions.

equilibrium sorption capacities for Cu^{2+} have been reported for various conventional and nanostructured materials in the literature.[32] As shown in the breakthrough curve (Fig. 5), 5 % breakthrough occurred at around 25 mL of cumulative effluent volume, while 95 % breakthrough was not attained even after 300 mL, indicating efficient Cu^{2+} retention and prolonged column performance. Throughout the tested volume, the removal efficiency remained consistently above 83 %, and the column utilization efficiency was calculated at 84.7 %. These results underscore the potential of the synthesized sorbent for scale-up, with further improvements expected through optimization of operational parameters such as flow rate, influent concentration, or bed depth.

Compared to conventional sorbents, the synthesized materials demonstrate several advantages: they utilize readily available mining byproducts, require no costly reagents or elaborate synthesis procedures, and exhibit sufficiently rapid kinetics to enable compact and efficient treatment systems. Although their sorption capacity is lower than that of advanced materials such as nano-hydroxyapatite,[33] the use of waste-derived precursors and simple processing offers a sustainable and economically viable alternative. Moreover, future enhancements, including hybrid modifications or surface functionalization, may further improve their performance for targeted environmental applications.

4. Conclusion

This study demonstrates the successful transformation of Akbakay gold ore processing waste into effective silicophosphate-based sorbents for the removal of Cu^{2+} from aqueous solutions. Through a combination of phosphoric acid modification and controlled thermal activation, the materials underwent substantial structural and surface changes, including the formation of phosphate phases, increased porosity, and enhanced negative surface charge—all of which contributed to improved adsorption performance. Among the synthesized materials, Sample 3 (600 °C, 20 wt.% H_3PO_4) exhibited the most favorable properties, achieving over 97% Cu^{2+} removal in batch experiments and a maximum equilibrium adsorption capacity of 1.33 mg/g. The sorption process was best described by the Langmuir isotherm model, indicating monolayer adsorption on a homogeneous surface, while kinetic analysis revealed a mixed-order mechanism involving both physisorption and chemisorption. Fixed-bed column studies further validated the material's practical potential, showing high retention efficiency, delayed breakthrough, and a dynamic sorption capacity of 0.847 mg/g. These findings underscore the viability of using phosphoric acid-modified mineral waste as a sustainable, low-cost, and scalable solution for heavy metal remediation. Future work should focus on the sorbents' regeneration capability, performance in complex wastewater matrices containing multiple contaminants, and pilot-scale implementation, particularly in mining-impacted regions where such waste materials are abundant and underutilized.

Acknowledgments

This research has been/was/is funded by the Science Committee of the Ministry of Education and Science of the Republic of Kazakhstan, grant number AP22685109.

Conflict of Interest

There is no conflict of interest.

Supporting Information

Applicable.

CRediT Statement

Sholpan Kubekova, Victoria Kapralova and Silviya Lavrova: Conceptualization. **Silviya Lavrova:** Formal analysis. **Arailym Kalymbet:** Project administration, Investigation, Funding acquisition. **Sholpan Kubekova, Victoria Kapralova and Silviya Lavrova:** Methodology. **Sholpan Kubekova and Victoria Kapralova:** Resources. **Arailym Kalymbet and Silviya Lavrova:** Software, Visualization, Writing—Review and editing. **Sholpan Kubekova and Arailym Kalymbet:** Supervision. **Arailym Kalymbet, Sholpan Kubekova, Victoria Kapralova and Silviya Lavrova:** Validation. **Arailym Kalymbet, Sholpan Kubekova and Victoria Kapralova:** Writing—Original draft preparation. All authors have read and agreed to the published version of the manuscript.

References

[1] F. Fu, Q. Wang, Removal of heavy metal ions from wastewaters: a review, *Journal of Environmental Management*, 2011, **92**, 407-418, doi: 10.1016/j.jenvman.2010.11.011.

[2] P. B. Tchounwou, C. G. Yedjou, A. K. Patlolla, D. J. Sutton, Heavy metal toxicity and the environment, *Molecular, Clinical and Environmental Toxicology*, Springer Basel, Basel, 2012, **101**, 133-164, doi: 10.1007/978-3-7643-8340-4_6.

[3] S. Babel, T. A. Kurniawan, Low-cost adsorbents for heavy metals uptake from contaminated water: a review, *Journal of Hazardous Materials*, 2003, **97**, 219-243, doi: 10.1016/S0304-3894(02)00263-7.

[4] G. Crini, E. Lichtfouse, Advantages and disadvantages of techniques used for wastewater treatment, *Environmental Chemistry Letters*, 2019, **17**, 145-155, doi: 10.1007/s10311-018-0785-9.

[5] A. A. Kubasov, Tseolity – kipjashhie kamni., Sorosovskii Obrazovatel'nyi Zhurnal, 2003, **7**, 70–76.

[6] L. M. Velichkina, L. L. Korobitsyna, and A. V. Vosmerikov, Sintez, kislotnye i kataliticheskie svoystva vysokokremnezemnykh tseolitov tipa ZSM-5, Neftepererabotka i Neftekhimiya, 2005, **10**, 32–35.

[7] G. S. Falkevich, N. N. Rostanin, and L. M. Vilensky, Vysokokremnezemnye tseolity v promyshlennosti., Kataliz v Promyshlennosti, 2002, **3**, 12–19.

[8] E. Dempsey, Acid strength and aluminum site reactivity of Y zeolites, *Journal of Catalysis*, 1974, **33**, 497-499, doi: 10.1016/0021-9517(74)90297-8.

[9] R. M. Barrer, Gidrotermal'naya Khimiya Tseolitov, 1985.
[10] T. V. Maltseva, A. G. Kotvitsky, and V. N. Belyakov, Svoystva neorganicheskikh kationoobmennykh membran na osnove fosfatsoderzhashchikh soedineniy, Khimiya i Tekhnologiya Vody, 2002, **24**, 526–534.
[11] K. G. Bhattacharyya, S. S. Gupta, Adsorption of a few heavy metals on natural and modified kaolinite and montmorillonite: a review, *Advances in Colloid and Interface Science*, 2008, **140**, 114-131, doi: 10.1016/j.cis.2007.12.008.
[12] Y. Shi, S. Zhong, X. Wang, C. Feng, A review of the removal of heavy metal ions in wastewater by modified montmorillonite, *Water Policy*, 2022, **24**, 1590-1609, doi: 10.2166/wp.2022.033.
[13] U. Kumar, M. Bandyopadhyay, Sorption of cadmium from aqueous solution using pretreated rice husk, *Bioresource Technology*, 2006, **97**, 104-109, doi: 10.1016/j.biortech.2005.02.027.
[14] S. Martini, S. Afroze, K. Ahmad Roni, M. Setiawati, D. Kharismadewi, A review of fruit waste-derived sorbents for dyes and metals removal from contaminated water and wastewater, *Desalination and Water Treatment*, 2021, **235**, 300-323, doi: 10.5004/dwt.2021.27658.
[15] O. Abdelwahab, W. M. Thabet, Natural zeolites and zeolite composites for heavy metal removal from contaminated water and their applications in aquaculture Systems: a review, *Egyptian Journal of Aquatic Research*, 2023, **49**, 431-443, doi: 10.1016/j.ejar.2023.11.004.
[16] M. Sulyman, J. Namiesnik, A. Gierak, Low-cost adsorbents derived from AgriculturalBy-products/wastes for enhancing ContaminantUptakes from wastewater: a review, *Polish Journal of Environmental Studies*, 2017, **26**, 479-510, doi: 10.15244/pjoes/66769.
[17] M. Kunarbekova, R. Busquets, I. Sapargali, *et al*., Synthesis and Characterization of Activated Carbon From Biomass, *Innovative Materials for Industrial Applications*, 2024, 329–348, doi: 10.4018/979-8-3693-7505-1.ch011.
[18] T. Alimbaev, Z. Mazhitova, C. Beksultanova, N. TentigulKyzy, Activities of mining and metallurgical industry enterprises of the Republic of Kazakhstan: environmental problems and possible solutions, *E3S Web of Conferences*, 2020, **175**, 14019, doi: 10.1051/e3sconf/202017514019.
[19] H. Argani, M. Latifa Bouamrani, S. Yousfi, M. Hammed El-Kouali, M. Talbi, R. Atmani, Adsorption process of Cu (II) cations by using the waste of phosphate rock (WPR) as novel adsorbent material, *Oriental Journal of Chemistry*, 2018, **34**, 1908-1918, doi: 10.13005/ojc/3404026.
[20] L. Zhou, L. Chen, Y. Zhang, Y. Zhang, Z. Li, K. Yang, L. Chen, The adsorption characteristics of phosphorus-modified corn stover biochar on lead and cadmium, *Agriculture*, 2024, **14**, 1118, doi: 10.3390/agriculture14071118.
[21] M. Mohery, G. M. A. Mahran, B. M. Atia, M. A. Gado, Removal of lead ions from wastewater by a new chelating amidoxime based-mesoporous silica, *Inorganic Chemistry Communications*, 2025, **180**, 114884, doi: 10.1016/j.inoche.2025.114884.
[22] S. A. Mahmoud, B. M. Atia, M. Abdalla, Polyvinyl alcohol-conjugated L-cysteine: a novel metal pincer for efficient heavy metal ions removal from wastewater, *ChemistrySelect*, 2024, **9**, e202401169, doi: 10.1002/slct.202401169.
[23] M. A. Gado, Efficient adsorption of thorium and cerium from Rosetta monazite concentrate using a novel phosphorylated Schiff-base adsorbent, *Journal of Radioanalytical and Nuclear Chemistry*, 2024, **333**, 5025-5048, doi: 10.1007/s10967-024-09667-4.
[24] S. A. Mahmoud, B. Mohamed, L. Galal Amin, M. Abdalla, Innovative pyrazole–phosphoramidate derivative for effective mercury adsorption and their application for Egyptian industrial waste samples, *International Journal of Environmental Analytical Chemistry*, 2024, 1-29, doi: 10.1080/03067319.2024.2385030.
[25] A. M. Amin, H. A. Ibrahium, A. A. Gouda, R. El Sheikh, B. M. Atia, M. A. Gado, N. S. Awwad, Design and utilisation of a novel poly imino-phosphorane composite for the effective removal of Pb^{2+} and Cr^{3+} ions from contaminated water sources, *International Journal of Environmental Analytical Chemistry*, 2024, 1-28, doi: 10.1080/03067319.2024.2420827.
[26] A. R. Weshahy, A. K. Sakr, A. A. Gouda, B. M. Atia, H. H. Somaily, M. Y. Hanfi, M. I. Sayyed, R. El Sheikh, E. M. El-Sheikh, H. A. Radwan, M. F. Cheira, M. A. Gado, Selective recovery of cadmium, cobalt, and nickel from spent Ni–Cd batteries using adogen® 464 and mesoporous silica derivatives, *International Journal of Molecular Sciences*, 2022, **23**, 8677, doi: 10.3390/ijms23158677.
[27] L. Wu, W. Wan, Z. Shang, X. Gao, N. Kobayashi, G. Luo, Z. Li, Surface modification of phosphoric acid activated carbon by using non-thermal plasma for enhancement of Cu(II) adsorption from aqueous solutions, *Separation and Purification Technology*, 2018, **197**, 156-169, doi: 10.1016/j.seppur.2018.01.007.
[28] G. T. Bare, J. J. K. Mbayo, S. Ndlovu, A. Shemi, L. Chipise, Mineralogical characterization and acid pretreatment of a gold calcine leach residue, *Minerals*, 2022, **12**, 10, doi: 10.3390/min12010010.
[29] S. Teimouri, J. H. Potgieter, G. S. Simate, L. van Dyk, M. Dworzanowski, Oxidative leaching of refractory sulphidic gold tailings with an ionic liquid, *Minerals Engineering*, 2020, **156**, 106484, doi: 10.1016/j.mineng.2020.106484.
[30] G. Jozanikohan, M. N. Abarghooei, The Fourier transform infrared spectroscopy (FTIR) analysis for the clay mineralogy studies in a clastic reservoir, *Journal of Petroleum Exploration and Production Technology*, 2022, **12**, 2093-2106, doi: 10.1007/s13202-021-01449-y.
[31] X. Chen, M. F. Hossain, C. Duan, J. Lu, Y. F. Tsang, M. S. Islam, Y. Zhou, Isotherm models for adsorption of heavy metals from water - A review, *Chemosphere*, 2022, **307**, 135545, doi: 10.1016/j.chemosphere.2022.135545.
[32] A. E. Burakov, E. V. Galunin, I. V. Burakova, A. E. Kucherova, S. Agarwal, A. G. Tkachev, V. K. Gupta, Adsorption of heavy metals on conventional and nanostructured materials for wastewater treatment purposes: a review, *Ecotoxicology and Environmental Safety*, 2018, **148**, 702-712, doi:

10.1016/j.ecoenv.2017.11.034.
[33] J. B. Dima, C. Sequeiros, N. E. Zaritzky, Hexavalent chromium removal in contaminated water using reticulated chitosan micro/nanoparticles from seafood processing wastes, *Chemosphere*, 2015, **141**, 100-111, doi: 10.1016/j.chemosphere.2015.06.030.

Publisher's Note: Engineered Science Publisher remains neutral with regard to jurisdictional claims in published maps and institutional affiliations.

Open Access
This article is licensed under a Creative Commons Attribution 4.0 International License, which permits the use, sharing, adaptation, distribution and reproduction in any medium or format, as long as appropriate credit to the original author(s) and the source is given by providing a link to the Creative Commons license and changes need to be indicated if there are any. The images or other third-party material in this article are included in the article's Creative Commons license, unless indicated otherwise in a credit line to the material. If material is not included in the article's Creative Commons license and your intended use is not permitted by statutory regulation or exceeds the permitted use, you will need to obtain permission directly from the copyright holder. To view a copy of this license, visit http://creativecommons.org/ licenses/by/4.0/.

©The Author(s) 2025.